Vortex flows impart chirality-specific lift forces

Thomas M. Hermans[1,†], Kyle J. M. Bishop[2], Peter S. Stewart[3,‡], Stephen H. Davis[3], Bartosz A. Grzybowski[1,*]

[1]Department of Chemical and Biological Engineering & Department of Chemistry, Northwestern University, 2145 Sheridan Rd., Evanston, IL 60208, USA.

[2]Department of Chemical Engineering, The Pennsylvania State University, 132C Fenske Lab, University Park, PA 16802, USA

[3]Engineering Sciences and Applied Mathematics, Northwestern University, Evanston, IL 60208, USA

*Correspondence and requests for materials should be addressed to BAG (grzybor@northwestern.edu)

[†]Current address: Institut de Science et d'Ingénierie Supramoléculaires (ISIS), 8 allée Gaspard Monge, 67000 Strasbourg, France

[‡]Current address: School of Mathematics and Statistics, University of Glasgow, University Gardens, Glasgow G12 0RB, UK

Around the turn of the 21st century, reports of macroscopic vortex flows discriminating between and forming chiral molecular assemblies sparked considerable scientific interest – indeed, the prospect of simple rotary evaporation inducing chiral selection could have profound implications for separations technologies and, above all, could shed new light on the origins of biological homochirality. Subsequently, however, these early results were put into question and attributed to either instrumental artifacts or even poor experimental control. After a decade of controversy, the question remains unresolved – how do vortex flows interact with different stereoisomers? Here, we implement a model experimental system to show that chiral objects placed in a vortex flow can indeed experience a chirality specific lift-force. Remarkably, this force is parallel to the shear plane which is in contrast to previous studies in which helices,

bacteria, and chiral cubes in shear flows were reported to experience forces perpendicular to the shear plane. In addition to experiments with macroscopic particles, we present a quantitative, hydrodynamic model that explains the origins of the chiral lift force and how it depends on particle size, shape, position, and flow velocity. The scaling laws derived here suggest that rotating flows can provide physical means of chiral separations at the micro- and nanoscales.

The idea that fluid flows can induce chiral migration was initially proposed by Howard *et al.*[1] and has since been examined theoretically in considerable detail.[2–10] Achieving separation of enantiomers[11,12] without the use of a chiral stationary phase – the most costly component in the separation process – would revolutionize the pharmaceutical industry. Surprisingly, however, there is still no agreement as to the magnitudes or even directions of forces affecting chiral objects in fluid flows.[7,10,13] Whereas several experimental studies report chirality-specific flow effects – on scales from molecular (porphyrin aggregation during rotary evaporation),[14,15] through microscopic (helical bacteria[2] and particles[16]), to macroscopic[13,17,18] – they remain largely phenomenological. Part of the problem is the possibly ambiguous interpretation of data,[19–21] e.g., from circular dichroism, and the experimental design in which vortex flows are implemented with imprecise systems such as rotary evaporators or magnetic stirrers,[22] for which the flow structure on different length-scales is largely unknown. We use the well-controlled flow generated in a Couette cell containing macroscopic chiral particles (confined to the liquid/air interface) to clarify the phenomenon of chiral migration. Importantly, by confining the motion of the particles to a two dimensional interface, we are able to capture the detailed rotational and translational motion of the particles in time – not just their average drifting motion as in previous studies[2,16,17]. Such detailed experimental data allows for quantitative comparisons with

predictions of the hydrodynamic model we develop.

Our experiments were performed in a custom-machined Couette cell (Fig. 1a,b) with the radius of the stationary inner cylinder $R_i = 25.4 \pm 0.01$ mm and that of the rotating outer cylinder $R_o = 55.9 \pm 0.01$ mm. The cylinders were aligned coaxially with the variation in the gap width, $G = R_o - R_i$, less than 0.5 mm. The cell was partially filled with paraffin oil (dynamic viscosity, $\eta = 0.17 \pm 0.06$ Pa·s; density, $\rho = 0.86 \pm 0.03$ g mL^{-1}) and in each experiment, a single millimeter-sized particle (7.70 × 2.46 × 0.20 mm, fabricated in SU-8 by photolithography; density 1.19 g mL^{-1}) was placed onto the oil/air interface such that it was fully immersed in the oil save for its top face (Fig. 1c). The particles we used were *s*-shaped (D_{2h} symmetry) such that when placed onto the interface, they could have two non-superimposable – that is, chiral – orientations, which we denote "R" and "S" (Fig. 1b) by analogy to chemical convention. A shear flow was generated in the cell by rotating the outer cylinder (a configuration for which Taylor instabilities cannot occur) at an angular frequency $\omega_{cell} = 1{-}3$ rad s^{-1}. For the typical particle dimensions and velocity, the particle Reynolds number was $\mathrm{Re} = \rho L R_o \omega_{cell} / \eta \sim 1$ where $L \approx 4$ mm is a characteristic linear dimension of the particle.

As the circular flow in the cell was established, the particles evolved within *ca.* 30 min to stable orbits. Importantly, the mean radii of these orbits depended on the particles' chirality (R,S) but not on the initial particle position. All particle trajectories were recorded and analyzed using house-written ImageJ and MATLAB scripts. The output of these scripts (*cf.* Fig. 1d) contained the linear velocity v_θ of the particle in the θ-direction, the angular velocity ω of the particle about its center, and the radial position r_c of the particle center measured from the axis of the Couette cell. Both R and S chiral particles revolved around the cell at a nearly constant speed v_θ with variations of only ~3% about the mean $\bar{v}_\theta$ (Fig. 1d, blue line). On the other hand, the R and S particles exhibited large periodic variations in their

angular velocities ω (Fig. 1d, red line) – the so-called Jeffery orbits[23] characteristic of elongated particles in shear flows.

The key experimental results of the present study are illustrated in Fig. 2a for R and S particles in either clockwise (CW) and counter-clockwise (CCW) directions of cell rotation. For CW rotation, the mean radius of the orbit traced by the R particles is always greater than that of the S particles in the same flow, $\overline{r}_c(R_{CW}) > \overline{r}_c(S_{CW})$. In contrast, in a CCW flow, the opposite is true and $\overline{r}_c(S_{CCW}) > \overline{r}_c(R_{CCW})$. Moreover, $\overline{r}_c(R_{CW}) \approx \overline{r}_c(S_{CCW})$ and $\overline{r}_c(R_{CCW}) \approx \overline{r}_c(S_{CW})$, which means that when the flow is reversed (from CW to CCW or from CCW to CW), the orbit of the R particle becomes that of S and *vice versa*. This last result leads to two conclusions: 1) It explicitly rules out any influence of particle shape imperfections, capillarity, *etc.*, on the orbit radius. The radii change when only the flow is reversed while the particles are not manipulated in any way. Additional evidence that capillary effects are negligible comes from confocal microscopy imaging (Fig. 1c), which shows no appreciable meniscus between the immersed particle and the surrounding fluid (note: even at the highest value of ω_{cell}, the inclination of the fluid interface due to centrifugal forces is less than one degree). 2) It indicates that the system can be treated as two-dimensional – indeed, under a hypothetical rotation of the Couette cell by 180 degrees around a horizontal/radial axis (Fig. 2b), the chirality of the particles and the directions of flow are both "reversed" with respect to a fixed observer (*e.g.*, R → S and CW → CCW in Fig. 2b) but the orbits should be invariant under this symmetry operation – as observed in experiments (hence, $\overline{r}_c(R_{CW}) \approx \overline{r}_c(S_{CCW})$ and $\overline{r}_c(R_{CCW}) \approx \overline{r}_c(S_{CW})$).

As expected for the Taylor–Couette flow (in which flow velocity increases with radial position, as given by Eq. **1** below), particles revolving around larger orbits have greater velocities v_θ – that is, $\overline{v}_\theta(R_{CW}) \approx \overline{v}_\theta(S_{CCW}) > \overline{v}_\theta(R_{CCW}) \approx \overline{v}_\theta(S_{CW})$ (hatched bars in Fig. 2c). At the same time, the average angular velocity $\overline{\omega}$ of a particle decreases with increasing radial

position – that is, $\bar{\omega}(R_{CW}) \approx \bar{\omega}(S_{CCW}) < \bar{\omega}(R_{CCW}) \approx \bar{\omega}(S_{CW})$ (solid bars in Fig. 2c,d) – because the shear rate $\dot{\gamma}$ decreases with increasing *r* and is itself linearly proportional to $\bar{\omega}$ as described by Jeffery[23]. Importantly, for achiral particles (disks or ellipsoids) no difference was observed in any of the measured variables (see section A of the supporting online information). Taken together, the above results indicate that the differences in the orbits of the R and S particles are due to their chirality. Because stable orbits correspond to the loci where all radial forces on the particles are balanced, we conclude that the R and S particles experience a lift force that is parallel to the shear plane (unlike in refs.2, 3, 7, 17) and whose direction depends on the chirality of the object with respect to the flow.

To gain further insight into the origin of this chiral lift, we considered a simplified hydrodynamic description, in which the chiral particles are modeled by rigid assemblies of *N* spheres each with radius *a* moving in the applied flow field **u**(**r**) (Fig. 3a). For the Taylor–Couette flow, **u**(**r**) is given by

$$\mathbf{u(r)} = \frac{R_i R_o^2 \omega_{cell}}{R_o^2 - R_i^2}\left(\frac{r}{R_i} - \frac{R_i}{r}\right)\mathbf{e}_\theta \qquad \textbf{[1]}$$

where $\mathbf{e}_\theta$ is the unit vector in the azimuthal direction. We begin by considering a description in which fluid inertia is negligible (*i.e.*, Re → 0, but see later in the text) and the movement of each sphere relative to the local fluid velocity **u** gives rise to a drag force $\mathbf{F}_i$ on sphere *i* of the form

$$\mathbf{F}_i = \sum_{j=1}^{N} \boldsymbol{\mathcal{R}}_{ij} \cdot \left(\mathbf{u}(\mathbf{r}_j) - \dot{\mathbf{r}}_j\right) \qquad \textbf{[2]}$$

where $\boldsymbol{\mathcal{R}}$ is the grand resistance matrix[24], which characterizes all hydrodynamic interactions between the *N* spheres that make up the composite particle. Provided that the spheres are small compared to the separation between them, the resistance matrix can be approximated by the inverse of the mobility matrix, $\boldsymbol{\mathcal{R}} = \boldsymbol{\mathcal{M}}^{-1}$, where $\boldsymbol{\mathcal{M}}$ has components

$$\mathcal{M}_{ii} = \frac{\boldsymbol{\delta}}{6\pi\eta a} \text{ and } \mathcal{M}_{ij} = \frac{1}{8\pi\eta}\left(\frac{\boldsymbol{\delta}}{\mathbf{r}_{ij}} + \frac{\mathbf{r}_{ij}\mathbf{r}_{ij}}{r_{ij}^3}\right) \text{ for } i \neq j \qquad \textbf{[3]}$$

where $\boldsymbol{\delta}$ is the identity tensor, and $\mathbf{r}_{ij} = \mathbf{r}_j - \mathbf{r}_i$ is the displacement vector between sphere *i* and *j* ($r_{ij} = |\mathbf{r}_{ij}|$). To maintain the relative distances between the spheres, the hydrodynamic forces are exactly balanced by intraparticle forces between the spheres such that the net force and torque on the particle are identically zero

$$\sum_i \mathbf{F}_i = \mathbf{0} \text{ and } \sum_i (\mathbf{r}_i - \mathbf{r}_c) \times \mathbf{F}_i = 0 \qquad \textbf{[4]}$$

where $\mathbf{r}_c$ is the position of the particle's center. Together with the kinematic conditions for rigid body motion, Eq. **2** and **4** govern the dynamics of the particle position $\mathbf{r}_c$ and its angular orientation (see supporting information, section B for details). This model is similar to that of Hänggi[6] and co-workers but includes hydrodynamic interactions between the spheres, which we found to have a significant impact on the magnitude of the chiral lift force and its scaling with particle size (see supporting information, section B3.5).

Numerical integration of the above equations provides several insights into the experimental observations (Fig. 3). First, the linear velocity of the particle is roughly constant and equal to that of the fluid evaluated at the particle's center, $v_\theta \approx u(r_c)$ (compare Figs. 1d and 3b). The angular velocity of the particle oscillates in time with a period equal to that of the particle's rotation (Fig. 3b); the period of these Jeffery orbits is well approximated as $T \approx \pi(\chi + \chi^{-1})/\dot{\gamma}$ where $\chi = 3.1$ is the aspect ratio of the particles, and $\dot{\gamma} = R_i^2 R_o^2 \omega_{cell} / r_c^2 (R_o^2 - R_i^2)$ is the shear rate. Despite the simplifications involved, the hydrodynamic model predicts the particle rotation period in quantitative agreement with experiment – *e.g.*, for $\omega_{cell} = 3$ rad s^{-1}, $T = 7.9$ s in experiment as compared to $T = 7.2$ s in the model using no tunable parameters.

Importantly, the radial position of the particle also oscillates in time but with a steady drifting motion that depends on both the chirality of the particle and the direction of the flow. For CCW rotation of the outer cylinder ($\omega_{cell} > 0$), S particles drift away from the origin while R particles drift toward the origin in agreement with experimental observations; the opposite behavior is observed for CW rotation. A detailed scaling analysis of the hydrodynamic model reveals that the chiral drift velocity v_c is well approximated as $v_c \approx \kappa aL / Tr_c$ where κ is a dimensionless "chiral factor" that characterizes the direction and magnitude of the chiral drift and depends only on the shape of the particle (see supporting information, section B3); for the model particles used in the simulations, $\kappa(S) = -\kappa(R) = 1.9$.

In the absence of inertial effects or hydrodynamic interactions with the walls of the Couette cell, chiral particles will drift monotonically towards or away from the center of the rotating flow. To understand the formation of the stable orbits observed in experiment, it is necessary to consider the role of fluid inertia, which acts to center the particle within the gap separating the concentric cylinders. Near the midline position, $r_0 = \frac{1}{2}(R_o + R_i)$, the inertial lift velocity v_i has been calculated previously[25] for spherical particles to be $v_i(r) \approx (r_0 - r)/\tau$ where $\tau \approx 36\eta G^3 / \rho\omega_{cell}^2 R_o^2 L^3$ is a characteristic time for the particle to relax to the steady-state orbit r_0. For chiral particles, the chiral drift velocity is expected to perturb the orbit of the particle away from r_0; the resulting steady-state orbit r_{ss} corresponds to that at which the chiral drift velocity balances the restoring lift velocity, $v_c(r_{ss}) \approx v_i(r_{ss})$. Using the above estimates, the difference in the steady-state orbits between R and S particles is estimated as $\Delta r_{ss} \approx \tau v_c(r_0) \sim 1$ mm and the relaxation time as $\tau \sim 10$ min both of which are in quantitative agreement with experiment. Interestingly, this mechanism also predicts that larger separations between chiral particles can be achieved at lower Reynolds numbers. This prediction is

supported by experiments that show that the chiral separation Δr_{ss} increases from 2.3 mm to 3.0 mm as the rotation speed is reduced by a factor of two (Fig. 2a).

Analysis of the hydrodynamic model reveals that chiral drift parallel to the shear plane occurs through a previously unreported mechanism requiring the presence of non-linear flow fields (*i.e.*, $\nabla\nabla\mathbf{u} \neq 0$). In general, the hydrodynamic force / torque $\mathcal{F}_H$ on a rigid particle depends both on its linear / angular velocity $\mathcal{U}$ and on the fluid velocity $\mathbf{u}$ as

$$\mathcal{F}_H = -\mathcal{R}_{FU} \cdot \mathcal{U} + \mathcal{C}_2 \cdot \mathbf{u}_o + \mathcal{C}_3 : (\nabla\mathbf{u})_o + \mathcal{C}_4 \vdots (\nabla\nabla\mathbf{u})_o + \ldots \qquad \textbf{[5]}$$

where $\mathcal{R}_{FU}$ is the particle resistance tensor, $\mathcal{C}_n$ are n^{th} order tensors that depend on the shape and size of the particle, and the velocity gradients are evaluated at the particle origin o.[26–29] To first approximation, a force and torque-free particle ($\mathcal{F}_H = 0$) moves at the local fluid velocity ($\mathbf{u}_o$) and rotates at a rate equal to one half the local fluid vorticity ($\frac{1}{2}\nabla\times\mathbf{u}_o$). Deviations of the particle's translational and rotational velocity from that of the fluid are caused by straining flows (*i.e.*, when $(\nabla\mathbf{u})_o + (\nabla\mathbf{u})_o^\dagger \neq 0$), which are incompatible with the rigid body motion of the particle. To describe these effects, it is most common to truncate the Taylor expansion of equation **[5]** at the level of velocity gradients and neglect higher order derivatives of the velocity field. This approximation has proven effective in describing the chiral drift of helical particles in linear shear flows along the direction normal to the shear plane.[2,7] By contrast, we find that chirality-dependent drifting motions in 2-dimensions require consideration of second order derivatives of the velocity field along with 4^{th}-order tensors ($\mathcal{C}_4$) to describe the detailed shape of the particle.

Physically, fluid shear within the Couette cell acts to rotate the particle about its center as it translates along a circular orbit. The interplay between rotation and orbital translation cause the particle to move back and forth along the radial direction perpendicular to the direction of flow (Fig. 3c). Each full rotation of the particle contributes a net

displacement that depends on the particle's chirality as quantified by the chiral factor κ. Although these drifting motions are typically small, their steady accumulation can lead to large displacements over many particle rotations and may therefore provide a basis for the hydrodynamic separation of chiral objects.

To assess the possibility of separating smaller micro- and nanoscale objects, we investigated the effect of Brownian motion on the chiral drift velocity through a series of stochastic simulations (see supporting information, section B4). Briefly, we added a fluctuating force / torque $\mathcal{F}_B$ with zero mean and covariance $\langle \mathcal{F}_B(0)\mathcal{F}_B(t)\rangle = 2k_BT\mathcal{R}_{FU}\delta(t)$ to the otherwise deterministic equations described above. The addition of these Brownian contributions introduced one additional parameter – namely, the thermal energy k_BT – which controlled the strength of thermal motion relative to the deterministic hydrodynamic motion of the particle. This parameter is conveniently expressed as the inverse of the Péclet number $Pe = v_c G / D$, where v_c is the chiral drift velocity *in the absence of Brownian motion*, $D = k_BT / K$ is a characteristic diffusion coefficient ($K = |\mathbf{K}|$ is the magnitude of the resistance tensor **K**; *e.g.*, $K = 6\pi\eta a$ for a sphere of radius a in an unbounded medium), and G is a length scale over which convection and diffusion are compared (*e.g.*, the gap width of a Taylor-Couette cell).

For each value of the Péclet number, we generated 1000 stochastic particle trajectories of duration $t_s = 10T$ (*i.e.*, 10 particle rotations) and calculated the resulting drift velocity, $v_{calc} = [r_c(t_s) - r_c(0)] / t_s$ (Figure 4). For weak thermal agitation ($Pe >> 1$), the average drift velocity $\langle v_{calc}\rangle$ agrees closely with the deterministic result, $\langle v_{calc}\rangle \approx v_c$. By contrast, for strong thermal agitation ($Pe << 1$) the particle trajectories are increasingly erratic such that displacement due to chiral drift is increasingly insignificant compared to that of Brownian motion. In the simulations, the length $G = v_c t_s$ was kept small for computational reasons (simulating the dynamics of microscopic particles over macroscopic lengths was

computationally prohibitive); however, the choice of G is arbitrary. Chiral drift (like any convective motion) will ultimately beat out diffusion over large length scales as displacement due to drift scales linearly with time whereas that due to diffusion scales as $t^{1/2}$. In other words, the Péclet number can be made increasingly large by increasing the length G over which the chiral separation is to occur. For a given length G, the separation of particles of opposite chirality should indeed be feasible provided that $Pe >> 1$ such that the effects of Brownian motion are small.

To separate objects over the gap width G of the Couette cell, transport due to chiral drift must exceed that due to diffusion: $v_c >> D / G$. Approximating the chiral drift velocity as $v_c \approx \kappa a L / Tr_c$ and the diffusivity as $D \approx k_B T / 3\pi\eta L$, this condition implies that the particle size must be $L >> (k_B T / \eta\omega_{cell})^{1/3}$ assuming the gap is small (*i.e.*, $G << R_o$). In water ($\eta = 10^{-3}$ Pa·s) at room temperature ($k_B T = 4\times10^{-21}$ J), a Couette cell rotating at rate of $\omega_{cell} = 10^3$ rad/s should be capable of separating chiral objects provided $L > 100$ nm. Separating even smaller chiral objects by this mechanism may also be possible in highly viscous fluids – for example, in glycerol ($\eta = 1$ Pa·s) the minimum size is $L > 10$ nm.

Interestingly, the chiral drift mechanism described here does not require the alignment of the particle along particular orientations (beyond the initial confinement to the interface) and is therefore insensitive to Brownian rotation. The flow induced rotation of the particle leads – on average – to more rotations in one direction than the other resulting in steady drifting motions. Over sufficiently long times (again corresponding to the condition, $Pe >> 1$), this steady rotational motion will always dominate that of Brownian motion. This behavior is in sharp contrast with previously reported mechanisms of chiral drift in 3-dimensions perpendicular to the shear plane,[2,7] which require the flow-induced alignment of the particles to achieve steady drifting motions. In these mechanisms, chiral drift vanishes at small scales due to Brownian rotation, which act to randomize the particle's orientation.

Thus, while the present mechanism is typically weaker than those described previously (*e.g.* v_c scales as L^2 as opposed to L), it may be more robust to Brownian motion at small scales.

In summary, we have provided conclusive evidence that particles in vortex flows experience in-plane lift forces that depend on particle chirality. This lift force does not vanish at the nanoscale, and should allow for the separation of chiral objects tens of nanometers across even in the presence of Brownian motion. ~~In extended three-dimensional systems, we expect the described in-plane lift force to act in addition to the known chiral lift force normal to the shear plane. Within a Couette cell, radial drift may also act to enhance chiral-selective motions normal to the shear plane by moving particles into regions with higher shear rate.~~ Although the present study focused exclusively on two-dimensional (2D) particles, in-plane lift forces should also act on 3D chiral objects provided they are confined at or near a liquid interface parallel to the shear plane. In the absence of such an interface, rotation of the Couette cell by 180° (cf. Fig. 2b) would reverse the apparent flow rotation direction but not the chirality of a 3D chiral particle; consequently, in-plane chiral lift forces are prohibited in extended Couette flows by symmetry considerations (see supporting information section D for an extended discussion). ~~To describe these effects,~~ In addition, future 3D models should incorporate the effects of higher order velocity gradients ($\nabla\nabla\mathbf{u}$), which may underlie potentially important mechanisms for the hydrodynamic separation of chiral objects. ~~Moreover~~ Lastly, the present experiments should be scaled down and extended to neutrally buoyant particles that can migrate and rotate in three dimensions; however, the implementation and imaging of such a system is expected to be significantly more challenging.

Acknowledgements:

This work was supported by the Non-equilibrium Energy Research Center which is an Energy Frontier Research Center funded by the U.S. Department of Energy, Office of Science, Office of Basic Energy Sciences under grant number DE-SC0000989. T.M.H. was funded by the Human Frontier Science Program. We acknowledge Prof. Alexander Z. Patashinski and Prof. Wesley R. Burghardt for helpful discussions.

Author contributions:

T.M.H. performed the experiments. K.J.M.B., T.M.H., P.S.S and S.H.D. developed the model and performed the simulations. B.A.G. conceived and supervised the project, and T.M.H., K.J.M.B., and B.A.G. wrote the paper.

Additional Information:

The authors declare no competing financial interests. Supplementary information accompanies this paper on xxxxx. Reprints and permission information is available online at xxxxx. Correspondence and requests for materials should be addressed to B.A.G.

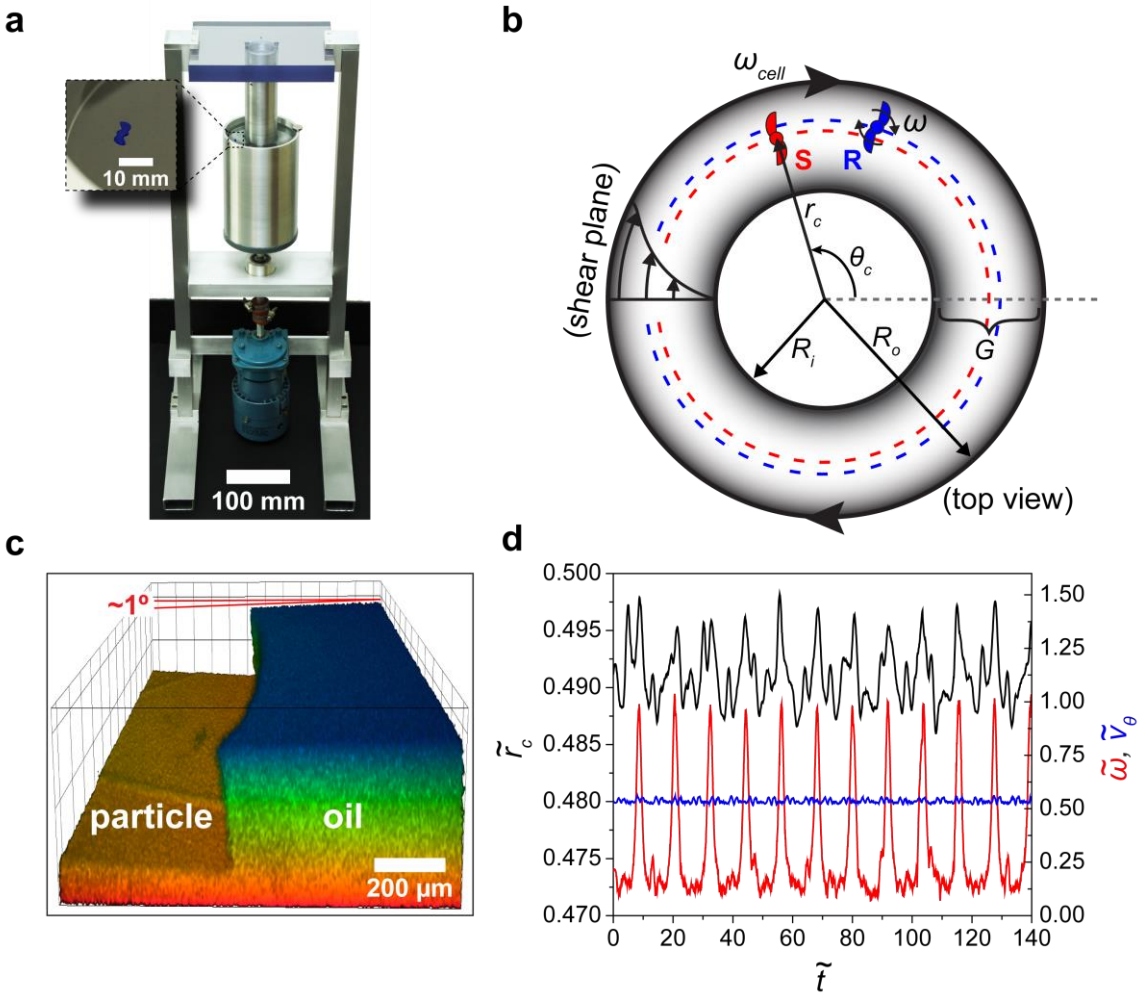

Figure 1 | Experimental arrangement. a, Optical image of the Couette cell with a millimeter sized chiral particle placed at the oil/air interface. **b,** Top-view scheme of the system with an inner cylinder stationary and an outer cylinder rotating – here, in the CW direction – at an angular velocity ω_{cell}. Two chiral particles (denoted R and S) are illustrated; these particles revolve around the cell with linear velocity v_θ and also rotate around their centers with an angular velocity ω. The shear plane is indicated by curved arrows. **c,** Three-dimensional confocal microscopy of a chiral particle floating stationary on top of paraffin oil (containing 1 μM diketopyrrolopyrrole to make the oil fluorescent). The particle is not fluorescent and therefore appears as a void space on the left of the image. No significant meniscus was observed (see supporting information, section C); the oil directly adjacent to the particle is downward sloping at a ~1° angle. The grid size is 50 × 50 μm. **d,** Typical experimental data showing the radial position $\tilde{r}_c = (r_c - R_i)/G$ (black), linear velocity $\tilde{v}_\theta = v_\theta / R_o\omega_{cell}$ (blue), and angular velocity $\tilde{\omega} = \omega/\omega_{cell}$ (red) of an S particle as a function of time $\tilde{t} = t\omega_{cell}$ (after particle reached a stable orbit); here, the cell velocity is ω_{cell} = 3.02 ± 0.13 rad s^{-1}.

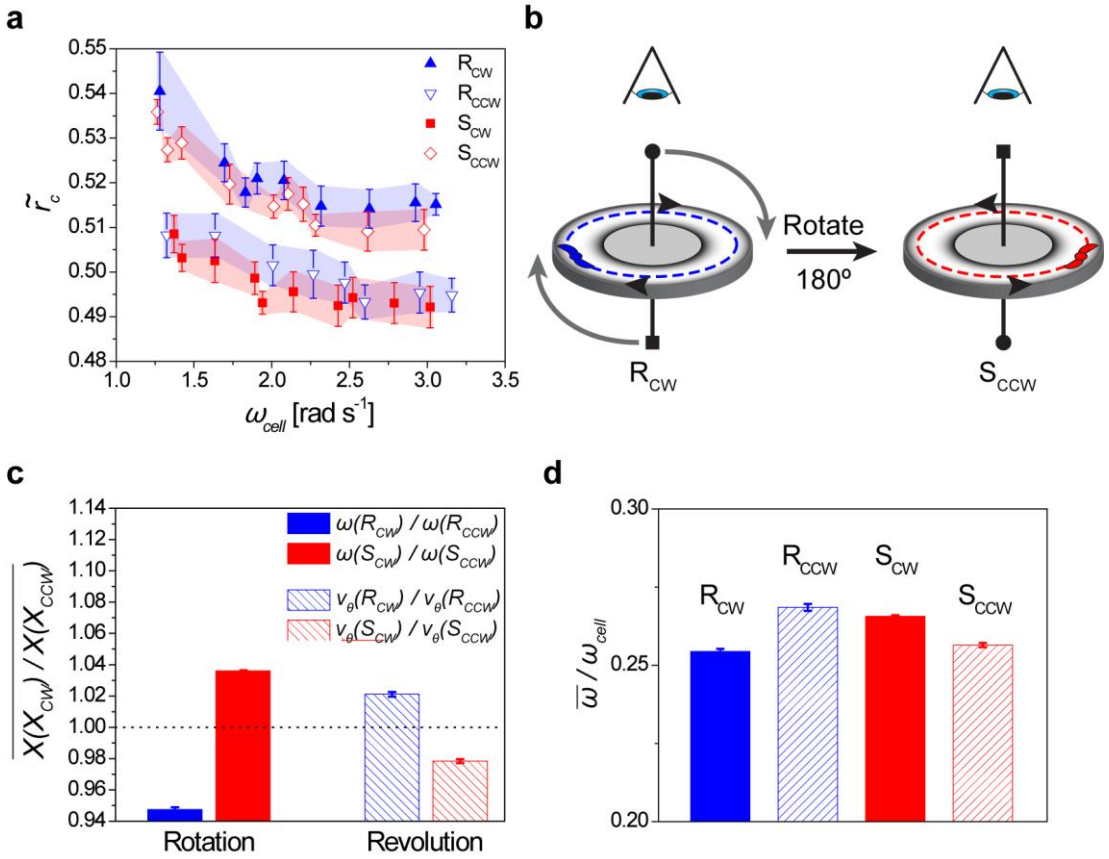

Figure 2 | Chirality effects in a vortex flow. a, The mean orbit radii $\tilde{r}_c = (\bar{r}_c - R_i)/G$ observed in experiments depends on the chirality of the particles and on the direction of flow (solid markers = CW cell rotation; open markers = CCW rotation). For all cell velocities ω_{cell}, $\tilde{r}_c(R_{CW}) > \tilde{r}_c(S_{CW})$ and $\tilde{r}_c(S_{CCW}) > \tilde{r}_c(R_{CCW})$. Upon "flow reversal" (without any manipulation of particles), $\tilde{r}_c(R_{CW}) \approx \tilde{r}_c(S_{CCW})$ and $\tilde{r}_c(R_{CCW}) \approx \tilde{r}_c(S_{CW})$. Error bars correspond to standard deviations in $\tilde{r}_c$, which are based on at least 10 independent experiments (12,500 data points per run recorded) for each value of ω_{cell} (note: four particles of each type were tested). **b,** Scheme illustrating why the behavior of a chiral particle in a CW flow is expected to be equivalent to its "mirror image" in a CCW flow. Rotation of the entire system about the horizontal/radial axis by 180° (denoted by grey arrows) changes particle chirality and flow direction (with respect to an observer along the vertical axis; denoted by an eye cartoon) – at the same time, the orbit radius remains unchanged. This is in agreement with the experimental observations in panel (a). **c,** When the direction of the flow changes from CW to CCW, not only the orbits of the chiral particles change, but so do the corresponding values of ω and v_θ. The bar graph illustrates this effect by plotting the averaged (over all experiments and ω_{cell} between 1 and 3 rad s^{-1}) values of the ratios of frequencies under CW and CCW flows. Error bars represent standard deviations based on at least 200 experiments for each bar. **d,** The frequency of rotation of the particles compared to that of the Couette cell averaged over all experiments (i.e. $\bar{\omega}/\omega_{cell}$).

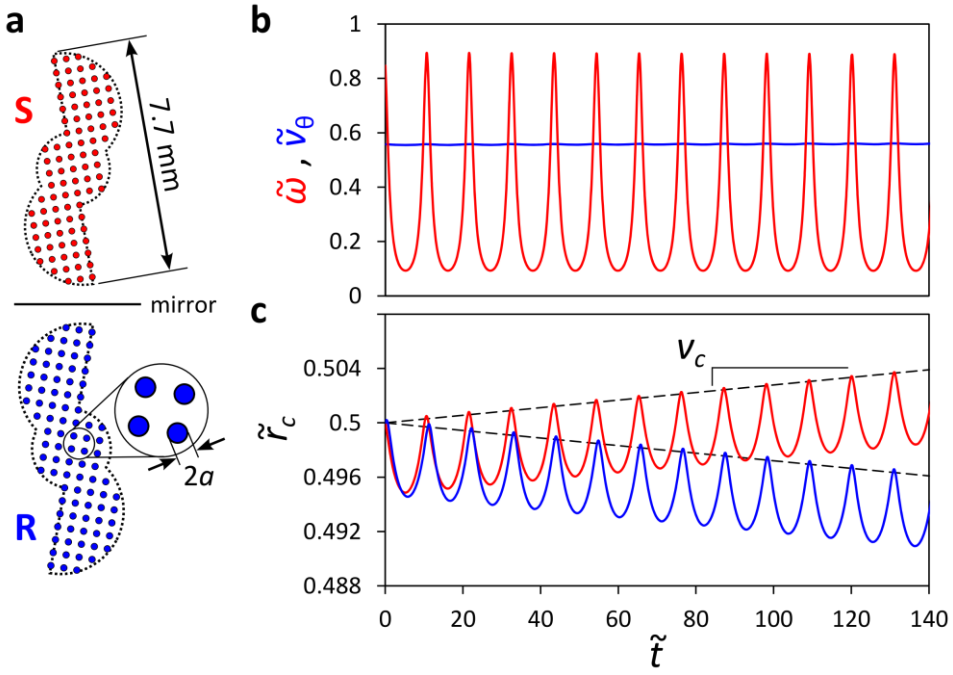

Figure 3 | Modeling of particle dynamics in a Taylor-Couette flow. a, Chiral particles (R and S) like those used in experiment are comprised of $N = 91$ spheres of radius $a = 0.1$ mm corresponding to the particle thickness; the spacing between neighboring spheres is $4a$. **b,** Numerical solution of the linear velocity $\tilde{v}_\theta = v_\theta / R_o\omega_{cell}$ and the angular velocity $\tilde{\omega} = \omega / \omega_{cell}$ of an S particle moving in a CCW flow as a function of time $\tilde{t} = t\omega_{cell}$. **c**, The radial position of the particle's center $\tilde{r}_c = (r_c - R_i)/G$ oscillates in time with a steady drifting motion whose direction depends on the chirality of the particle.

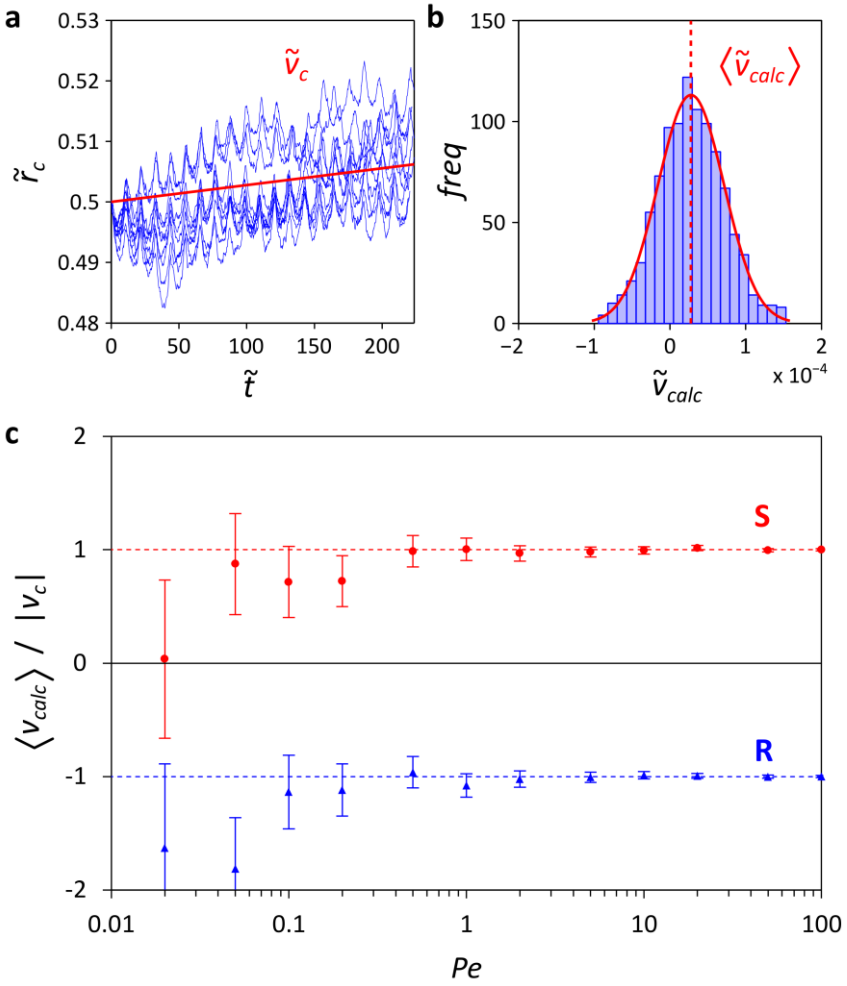

Figure 4 | Stochastic particles simulations. a, 10 (of 1000) stochastic particle trajectories of an R particle (Fig. 3a) for Peclét number, $Pe = 1$. **b,** Histogram showing the corresponding distribution of drift velocities v_{calc} defined in the main text for $Pe = 1$. **c,** Average drift velocity $\langle v_{calc} \rangle$ as a function of Pe for chiral particles (R and S) shown in Fig. 3a. The error bars represent 95% confidence intervals on the mean drift velocity based on 1000 realizations of the stochastic process.

References

1. Howard, D. W., Lightfoot, E. N. & Hirschfelder, J. O. The hydrodynamic resolution of optical isomers. *AIChE Journal* **22,** 794–798 (1976).
2. Marcos, Fu, H. C., Powers, T. R. & Stocker, R. Separation of microscale chiral objects by shear flow. *Phys. Rev. Lett.* **102,** 158103 (2009).
3. Chen, P. & Zhang, Q. Dynamical solutions for migration of chiral DNA-type objects in shear flows. *Phys. Rev. E* **84,** 056309 (2011).
4. Eichhorn, R. Enantioseparation in microfluidic channels. *Chem. Phys.* **375,** 568–577 (2010).
5. Gennes, P. G. de. Mechanical selection of chiral crystals. *Europhys. Lett.* **46,** 827–830 (1999).
6. Kostur, M., Schindler, M., Talkner, P. & Hänggi, P. Chiral separation in microflows. *Phys. Rev. Lett.* **96,** 014502 (2006).
7. Makino, M. & Doi, M. Migration of twisted ribbon-like particles in simple shear flow. *Phys. Fluids* **17,** 103605 (2005).
8. Tencer, M. & Bielski, R. Mechanical resolution of chiral objects in achiral media: Where is the size limit? *Chirality* **23,** 144–147 (2010).
9. Watari, N. & Larson, R. G. Shear-induced chiral migration of particles with anisotropic rigidity. *Phys. Rev. Lett.* **102,** 246001 (2009).
10. Kim, Y.-J. & Rae, W. J. Separation of screw-sensed particles in a homogeneous shear field. *Int. J. Multiphas. Flow* **17,** 717–744 (1991).
11. Maier, N. M., Franco, P. & Lindner, W. Separation of enantiomers: needs, challenges, perspectives. *J. Chromatogr. A* **906,** 3–33 (2001).
12. Pirkle, W. H. & Pochapsky, T. C. Considerations of chiral recognition relevant to the liquid chromatography separation of enantiomers. *Chem. Rev.* **89,** 347–362 (1989).
13. Chen, P. & Chao, C.-H. Lift forces of screws in shear flows. *Phys. Fluids* **19,** 017108 (2007).
14. Ribó, J. M. Chiral sign induction by vortices during the formation of mesophases in stirred solutions. *Science* **292,** 2063–2066 (2001).
15. Rubires, R., Farrera, J.-A. & Ribó, J. M. Stirring effects on the spontaneous formation of chirality in the homoassociation of diprotonated meso-tetraphenylsulfonato porphyrins. *Chemistry* **7,** 436–446 (2001).

16. Aristov, M., Eichhorn, R. & Bechinger, C. Separation of chiral colloidal particles in a helical flow field. *Soft Matter* **9,** 2525–2530 (2013).
17. Makino, M., Arai, L. & Doi, M. Shear migration of chiral particle in parallel-disk. *J. Phys. Soc. Jpn.* **77,** 064404 (2008).
18. Grzybowski, B. A. & Whitesides, G. M. Dynamic aggregation of chiral spinners. *Science* **296,** 718 –721 (2002).
19. Mead, C. A. & Moscowitz, A. Some comments on the possibility of achieving asymmetric synthesis from achiral reactants in a rotating vessel. *J. Am. Chem. Soc.* **102,** 7301–7302 (1980).
20. Wolffs, M. *et al.* Macroscopic origin of circular dichroism effects by alignment of self-assembled fibers in solution. *Angew. Chem. Int. Ed.* **46,** 8203–8205 (2007).
21. Amabilino, D. B. Supramolecular assembly: Nanofibre whirlpools. *Nat. Mater.* **6,** 924–925 (2007).
22. Crusats, J., El-Hachemi, Z. & Ribó, J. M. Hydrodynamic effects on chiral induction. *Chem. Soc. Rev.* **39,** 569 (2010).
23. Jeffery, G. B. The motion of ellipsoidal particles immersed in a viscous fluid. *P. R. Soc. Lond. A-Conta.* **102,** 161–179 (1922).
24. Kim, S. & Karrila, S. J. *Microhydrodynamics : principles and selected applications*. (Dover Publications, Mineola, N.Y., 2005).
25. Ho, B. P. & Leal, L. G. Inertial migration of rigid spheres in two-dimensional unidirectional flows. *J. Fluid Mech.* **65,** 365–400 (1974).
26. Brenner, H. The Stokes resistance of an arbitrary particle. *Chem. Eng. Sci.* **18,** 1–25 (1963).
27. Brenner, H. The Stokes resistance of an arbitrary particle--II : An extension. *Chem. Eng. Sci.* **19,** 599–629 (1964).
28. Brenner, H. The Stokes resistance of an arbitrary particle--III : Shear fields. *Chem. Eng. Sci.* **19,** 631–651 (1964).
29. Brenner, H. The Stokes resistance of an arbitrary particle--IV Arbitrary fields of flow. *Chem. Eng. Sci.* **19,** 703–727 (1964).